AIAA SciTech Forum
8-12 January 2024, Orlando, FL
AIAA SCITECH 2024 Forum

10.2514/6.2024-1320

Simulation of 3D Flapped Co-Flow Jet Airfoil with Quasi-Micro-Compressor from Low Speed to Cruise

Paula A. Barrios [*] Yan Ren [†] GeCheng Zha [‡]
Dept. of Mechanical and Aerospace Engineering
University of Miami, Coral Gables, Florida 33124
E-mail: gzha@miami.edu

December 10, 2023

Abstract

This paper presents a 3D flapped co-flow jet (FCFJ) airfoil with a quasi-micro-compressor to study the performance at different operating conditions within the flight envelope from low speed takeoff/landing to cruise. The FCFJ airfoil has a flap of 60%C with CFJ implemented on the flap as part of the airfoil. CFJ injection and suction ducts are designed for the cruise condition of Mach 0.25 with a flap deflection angle (β) of 10°, which corresponds to an angle of attack (AoA) of 7°. The FCFJ airfoil has an injection and suction duct that has a circular interface with the micro-compressor and transitions to a rectangle slot at the airfoil. Design iteration of the ducts is an important step in the integration of CFJ airfoil and micro-compressor by matching the mass flow rate and compressor total pressure ratio. The micro-compressor is represented by compressor boundary conditions provided by the compressor design and is therefore a quasi-micro-compressor. The purpose is to understand how the aerodynamic performance of the FCFJ varies as the airfoil flap deflection angle (β) is changed from an initial position of 70° at takeoff to 10° at cruise.

The takeoff condition is at low speed with a freestream Mach of 0.07 for $\beta = 60°$ and $70°$. As β is decreased from takeoff toward the cruise condition, the freestream Mach number is increased to Mach 0.17 for $\beta = 30°$, 40°, and 50°, and then to Mach 0.25 for $\beta = 0°$, 5°, 10°, 15°, and 20°. Results show both the lift coefficient (C_L) and the drag coefficient (C_D) decreasing as β varies from takeoff to cruise. A high C_L of 6.9 occurs at takeoff $\beta = 70°$ with an AoA of 50°. The lowest CFJ power coefficient (P_c) occurs at the cruise condition of Mach 0.25 and $\beta = 10°$, which is selected as the cruise condition with an AoA of 7°, lift coefficient C_L of 1.77, C_L/C_D of 89.8, $(C_L/C_D)_c$ of 44.6, and C_L^2/C_{D_c} of 79.2. The highest corrected aerodynamic efficiency (C_L/C_{D_c}) is 45.5 at cruise Mach 0.25 and $\beta = 15°$. This study demonstrates that it is feasible to use the FCFJ airfoil for the entire flight envelope for short takeoff/landing with high lift coefficient and cruise with high aerodynamic efficiency and productivity efficiency.

Nomenclature

$FCFJ$	Flapped Co-flow jet
CFJ	Co-flow jet
AoA	Angle of attack
β	Flap Deflection Angle
LE	Leading Edge
TE	Trailing Edge

---

[*] Ph.D. Candidate

[†] Researcher. Ph.D., AIAA member

[‡] Professor, ASME Fellow, AIAA associate Fellow

S	Planform area
s	Wing Span length
c	Profile chord
U	Flow velocity
q	Dynamic pressure, $0.5\,\rho\,U^2$
p	Static pressure
ρ	Air density
$\dot{m}$	Mass flow rate
M	Mach number
ω	Pitching Moment
P	Pumping power
∞	Freestream conditions
C_L	Lift coefficient, $L/(q_\infty\,S)$
C_D	Drag coefficient, $D/(q_\infty\,S)$
C_M	Pitching moment coefficient
C_μ	Jet momentum coefficient, $\dot{m}_j\,U_j/(q_\infty\,S)$
Pc	Power coefficient, $P/(q_\infty\,S\,V_\infty)$
η	Micro-compressor total-to-total efficiency
(C_L/C_D)	Airfoil aerodynamic efficiency
$(C_L/C_D)_c$	CFJ airfoil corrected aerodynamic efficiency, $C_L/(C_D+P_c)$
$(C_L^2/C_D)_c$	CFJ airfoil cruise productivity efficiency

1 Introduction

The most important phase of an aircraft's flight envelope is typically the cruise flight to achieve high mission effectiveness, long range, and high transportation capacity (i.e., payload × range). An aircraft at cruise must fly with a high aerodynamic efficiency, C_L/C_D, while maintaining a sufficient stall margin. The takeoff and landing phase of an aircraft requires a high lift coefficient, particularly if a short takeoff and landing distance is desired. With multi-element flaps, conventional high-lift wings can get a maximum lift coefficient of around 2.5. No aircraft would cruise at such a high lift coefficient since the aircraft would be near stall and the very large drag coefficient would make most of the missions unfeasible. However, active flow control (AFC) makes an ultra-high cruise lift coefficient possible.

AFC transfers external energy to the controlled flow to improve the performance of the flow system. For all AFC systems, there are three measures of merit (MoM): 1) effectiveness, 2) power required (PR), and 3) power conversion efficiency (PCE). Effectiveness quantifies performance enhancement, e.g., removal of flow separation, drag reduction, lift increase, stall prevention, noise mitigation, etc. Power required quantifies the AFC power needed to achieve the targeted effectiveness. Power conversion efficiency quantifies the efficiency to convert the external energy (e.g., mechanical, electric, chemical) to energy required by the controlled flow. It determines how much total power will be consumed by the actual flow control system. For AFC to benefit industry realistic applications, all three MoM matter. The ultimate criterion for an AFC is that the system efficiency gain should be greater than the AFC energy expenditure.

Co-flow jet (CFJ) active flow control airfoil, in Figure 1, is shown to have high effectiveness and high energy efficiency [1, 2, 3, 4, 5, 6, 7, 8, 9, 10, 11], which are attributed to three essential factors: 1) zero-net-mass-flux as a self-contained system; 2) micro-compressor fluidic actuators with high jet momentum and high energy conversion efficiency; 3) immersed in adverse pressure gradient region with the injection near separation onset location. For the CFJ AFC, an injection slot near the leading edge (LE) and a suction slot near the trailing edge (TE) on the airfoil suction surface are created. A small amount of mass flow is withdrawn into the suction slot located near the TE, pressurized and energized by the micro-compressor, and injected near the LE tangentially to the main flow through the injection slot. CFJ is able to achieve high effectiveness and low power required. The actual power consumed by the micro-compressor is $P_{act} = P_c/\eta$, where P_c is the required power coefficient and η is the micro-compressor power conversion efficiency.

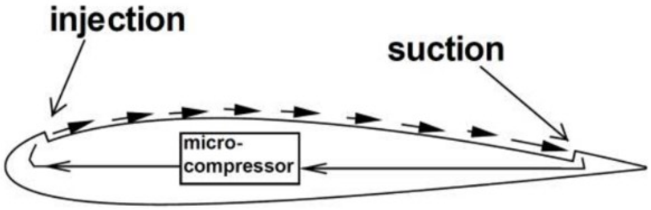

Figure 1: 2D sketch of CFJ airfoil showing the flow direction

CFJ airfoil can achieve very high maximum lift coefficient exceeding the theoretical limit of $C_{Lmax} = 2\pi(1+t/c)$ up to 13 and beyond [12, 13, 14, 15]. However, for cruise condition, the regular 3D CFJ configuration with the embedded compressor as shown in Figure 2 appears to have rapid energy consumption increase when C_L is greater than 1.6 [12, 16]. Even though the aerodynamic drag coefficient C_D can remain small and the pure aerodynamic lift to drag ratio C_L/C_D can still be very high, the corrected aerodynamic efficiency (C_L/C_{D_c}) can decrease quickly with the increasing C_L when it is greater than 1.6.

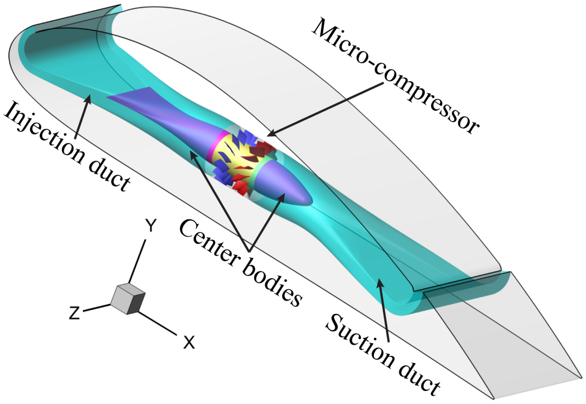

Figure 2: Schematic of 3D CFJ airfoil with embedded micro-compressor and ducts

To push the cruise lift coefficient higher, Jeon et al. [17] determined that the 2D airfoil with co-flow jet applied on the flap is a promising candidate that can potentially maintain an acceptable aerodynamic efficiency of C_L/C_{D_c}. Such an airfoil is named a flapped CFJ airfoil that is originated from the deflected slipstream study for VTOL aircraft [18].

1.1 Flapped Co-Flow Jet (FCFJ) Airfoil

The concept of a flapped co-flow jet airfoil is adopted from the CFJ airfoil with deflected slipstream for VTOL aircraft [18]. It is also guided by the co-flow jet flow separation mechanism study of Xu and Zha [19]. The CFJ is applied inside a long flap, 60%C, that is a part of the flapped CFJ airfoil as shown in Figure 3 [17], which has the injection located at the shoulder of the flap. The regular CFJ airfoil applies the injection very close to the leading edge at a point of around 2-4%C. By deflecting the flap rather than rotating the front of the airfoil, the FCFJ airfoil has the advantage of allowing the airfoil to change the angle of attack (AoA) and lift coefficient without tilting the wings or the aircraft. The goal is to analyze the aerodynamic performance of a 3D FCFJ airfoil from low speed takeoff/landing to cruise.

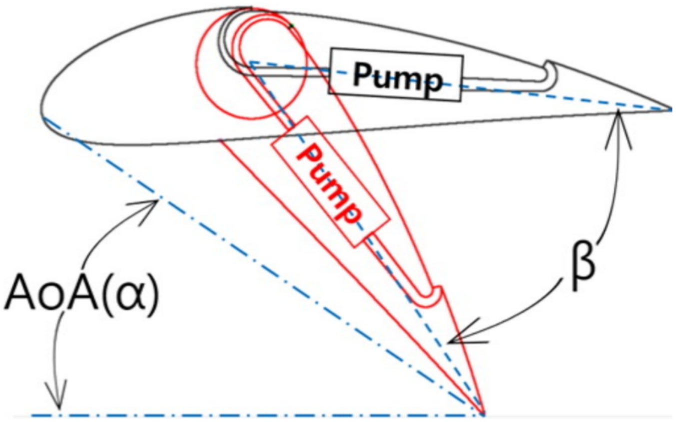

Figure 3: Schematic of flapped CFJ airfoil with CFJ applied at the flap

2 Methodology

2.1 Lift and Drag Calculation

In a CFD analysis of a CFJ airfoil, the total aerodynamic forces and moments are determined by the force surface integral and jet reactionary force. The reactionary force of a CFJ airfoil is calculated through flow parameters obtained from the injection and suction slots. The equations for lift and drag due to the jet reactionary force are given by Zha et al. [2] using the control volume analysis in Figure 4:

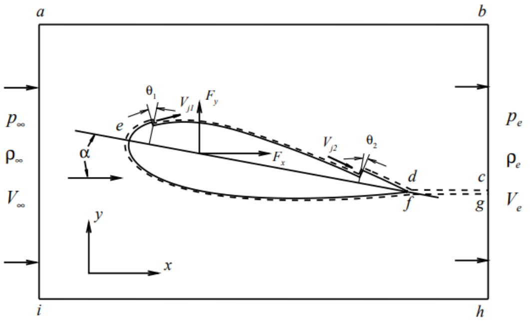

Figure 4: Control volume of a CFJ airfoil

$$F_{x_{cfj}} = (\dot{m}_j V_{j1} + p_{j1} A_{j1}) * cos(\theta_1 - \alpha) - (\dot{m}_j V_{j2} + p_{j2} A_{j2}) * cos(\theta_2 + \alpha) \tag{1}$$

$$F_{y_{cfj}} = (\dot{m}_{j1} V_{j1} + p_{j1} A_{j1}) * sin(\theta_1 - \alpha) + (\dot{m}_{j2} V_{j2} + p_{j2} A_{j2}) * sin(\theta_2 + \alpha) \tag{2}$$

where the subscript 1 indicates the injection slot and subscript 2 denotes the suction slot, θ_1 and θ_2 are the angles between the slot's surface and a line normal to the chord, and α is the angle of attack.

Total lift and drag are given by the following equations:

$$D = R'_x - F_{x_{cfj}} \tag{3}$$

$$L = R'_y - F_{y_{cfj}} \tag{4}$$

where R'_x and R'_y are surface integrals of pressure and shear stress in the x_{drag} and y_{lift} directions. For a 3D CFJ wing, total lift and drag are determined by integrating the drag and lift equations in the span wise direction.

2.2 Jet Momentum Coefficient

C_μ, or the jet momentum coefficient, quantifies the jet intensity and is defined by,

$$C_\mu = \frac{\dot{m}V_j}{\frac{1}{2}\rho_\infty {V_\infty}^2 S} \tag{5}$$

where $\dot{m}$ is the injection mass flow rate, V_j is the mass-averaged injection velocity, ρ_∞ is the free stream density, V_∞ is the free stream velocity, and S is the planform area.

2.3 Micro-Compressor Power Coefficient

In a CFJ airfoil, a system of micro-compressors are embedded inside of the wing. The micro-compressors take air from the suction slot and and eject the air through the injection slot. The power consumption is determined by the jet mass flow and total enthalpy change through:

$$P_c = \dot{m}(H_{t1} - H_{t2}) \tag{6}$$

where H_{t1} and H_{t2} are the mass-averaged total enthalpy in the injection and suction slots, P is the power required by the micro-compressor, and $\dot{m}$ the jet mass flow rate. The power consumption of Eq. (6) can be also expressed by the following equation,

$$P_c = \frac{\dot{m}C_p T_{t2}}{\eta}(\Gamma^{\frac{\gamma-1}{\gamma}} - 1) \tag{7}$$

where γ is the specific heat ratio, or 1.4 for ideal gas, and η is the isentropic pumping efficiency. Γ is the total pressure ratio of the pump defined as $\Gamma = \frac{P_{t1}}{P_{t2}}$, where P_{t1} and P_{t2} are the mass-averaged total pressures in the injection and suction slots, respectively. The power coefficient for a CFJ airfoil is then,

$$P_c = \frac{P}{\frac{1}{2}\rho_\infty V_\infty^3 S} \tag{8}$$

2.4 Corrected Aerodynamic Efficiency

For a conventional airfoil, the wing aerodynamic efficiency is defined as:

$$\frac{L}{D} \tag{9}$$

and for a CFJ wing, the pure aerodynamic relationship between lift and drag still follows Eq. 9. However, since CFJ AFC expends energy, the above is modified to consider the energy consumption of the micro-compressor. The corrected aerodynamic efficiency is:

$$\frac{C_L}{C_{Dc}} = \frac{C_L}{C_D + P_c} \tag{10}$$

where C_{Dc} is the equivalent drag coefficient that includes the drag of the aircraft system and the power required by the CFJ.

2.5 Aircraft Productivity

The productivity efficiency C_L^2/C_D is used to measure the productivity of an airplane characterized by the product of an aircraft's range and its weight [12]. It is a more thorough parameter than C_L/C_D in determining the merit of aerodynamic design during cruise. Aircraft productivity includes the ratio of lift to drag coefficient and the aircraft weight from C_L. The corrected productivity efficiency for CFJ airfoils is defined as,

$$\frac{C_L^2}{C_{Dc}} = \frac{C_L^2}{C_D + P_c} \tag{11}$$

2.6 Airfoil Geometry

The airfoil is developed based on the NACA 6421 airfoil. The CFJ injection and suction slot sizes are normalized by the airfoil chord length (C). The flapped CFJ6421-SST150-SUC133-INJ040 designed by Jeon et al. [17] has a suction surface translation (SST) of 1.50%C, a suction slot size of 1.33%C, and an injection slot size of 0.4%C.

2.7 Duct Geometry

The ducts have a circular shape at the compressor interface and then become rectangular at the slots. The method of calculating circular-to-rectangular transition surfaces developed in [20] is adopted. The CFJ airfoil injection and suction slot locations are determined according to previously published 2D designs [21, 16, 22]. The injection and suction duct meanlines are determined based on the slot locations. Superellipses are created along the duct meanlines, which pass through the superellipse geometric centers and locally perpendicular to the superellipses. The duct surfaces are formed by connecting those cross sections.

Converging ducts have a favorable pressure gradient and are easier to design than diverging ducts, which are prone to flow separation. When designing the ducts, the center bodies design is important for both the injection and suction duct since they are used to guide the flow entering and exiting the micro-compressor and prevent flow separation. Key parameters in CFJ duct design are the area distribution and the ratio of the slot width to the compressor diameter, W/D.

Duct design is an integral part of the optimization of the system, requiring as high as possible total pressure recovery without flow separation. Total pressure recovery of a CFJ duct is defined as,

$$P_{tr} = \frac{\oiint_{S_o} \rho V P_{02} dA}{\oiint_{S_i} \rho V P_{01} dA} \tag{12}$$

where S_o and S_i are the cross section interface of the CFJ duct at outlet and inlet respectively. P_{02} and P_{01} are the total pressure evaluated at outlet and inlet. A high total pressure recovery signifies minimal loss within the duct. For injection ducts, the total pressure decreases toward the injection slot while for suction ducts the total pressure decreases toward the compressor interface.

2.8 CFD Simulation Setup

The FASIP (Flow-Acoustics-Structure Interaction Package) CFD code is used for the numerical simulation and design. The 3D Improved Delayed Detached Eddy Simulation (IDDES) turbulence model is used for take-off/landing conditions while the 3D Reynolds Averaged Navier-Stokes (RANS) equations with one-equation Spalart-Allmaras [23] turbulence model is used for the cruise conditions. A 3rd order WENO scheme for the inviscid flux [24, 25, 26, 27, 28, 29] and 2nd order central differencing for the viscous terms [24, 28] are utilized to discretize the Navier-Stokes equations. The low diffusion Roe scheme used as the approximate Riemann solver is utilized with the WENO scheme to evaluate the inviscid fluxes. Implicit time marching method using Gauss-Seidel line relaxation is used to achieve a fast convergence rate [30]. Parallel computing is implemented to save wall clock simulation time [31].

2.9 Boundary Conditions

Examples of the computational mesh used are in Figure 5, showing the designed injection and suction ducts at the flap. The meshes shown have a flap deflection angle of 10° and 70°. The far field boundary is located at 55 chord lengths with an O-mesh topology. The 3rd order accuracy no slip condition is enforced on the solid surface with the wall treatment suggested in [32] to achieve flux conservation on the wall. Symmetric boundary conditions are utilized on the two boundaries in the span direction. Total pressure, total temperature and flow angles are specified at the injection duct inlet based on the profile of the micro-compressor at the outlet. The total pressure, total temperature, and flow angle are also specified at the upstream portion of the far field based on free stream condition. Constant static pressure is applied at the suction duct outlet as well as the downstream portion of the far field. The total mesh size for the FCFJ airfoil is 3.52 million points, split into 88 blocks for the parallel computation. The first grid point on the wing surface is placed at $y^+ \approx 1$.

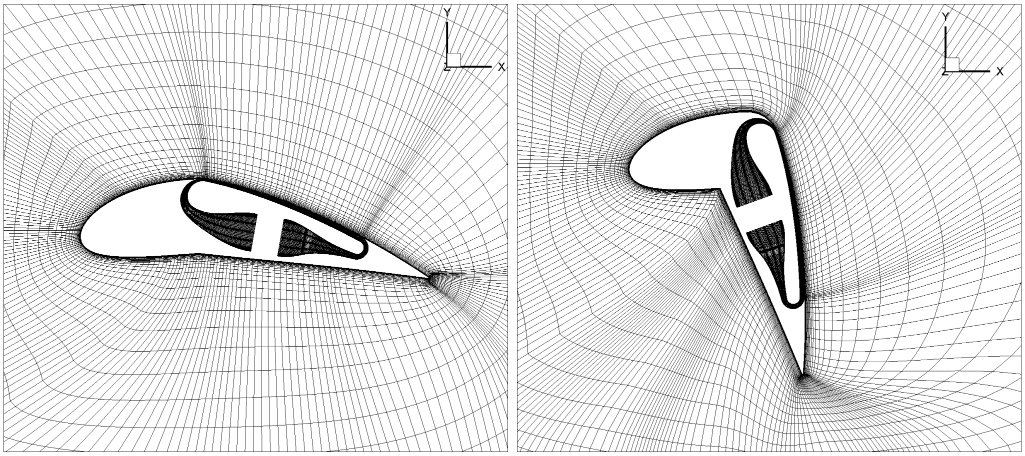

(a) (b)

Figure 5: Example of computational mesh used at (a)$\beta = 10^\circ$ and (b)$\beta = 70^\circ$

2.10 Integrated Design Procedure

The integrated design steps are as follows:

1. CFJ wing design: 2D CFJ airfoil and 3D CFJ wing are designed to meet the aircraft mission requirements for takeoff, cruise, and landing with optimal performance. The design provides the requirements of wing dimensions, micro-compressor mass flow rate, and total pressure ratio.

2. Micro-compressor design: A micro-compressor is then designed to satisfy the required total pressure ratio and the dimensions of the airfoil with maximized mass flow rate, highest efficiency, and largest operating range from choke limit to stall limit.

3. Duct design: The CFJ injection and suction ducts are then designed to match the airfoil dimensions with the boundary conditions from the micro-compressor and the CFJ wing flow conditions, no flow separation inside the ducts, and minimum total pressure loss.

4. Integrate the designed ducts with the 3D CFJ airfoil and the micro-compressor connected to the CFJ injection inlet (micro-compressor outlet) and suction outlet (micro-compressor inlet).

5. Examine the results and the aerodynamic performance. If satisfied, the design is complete; if not satisfied, return to Step 1 and repeat the process. However, to save time, Step 2 of the compressor design is not iterated in this study and is only conducted at the beginning. Thus the micro-compressor is a quasi-micro-compressor.

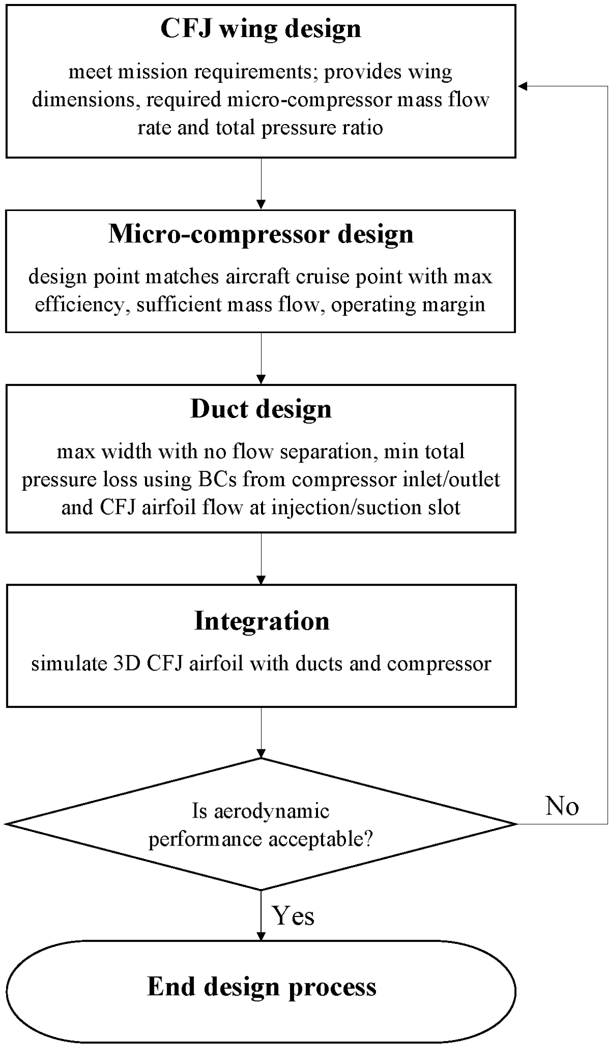

Figure 6: Flowchart of the integrated design process

3 Results and Discussion

3.1 Micro-Compressor

The following table describes the parameters of the micro-compressor utilized in this study. During duct design iterations it was observed that flow separation occurred at the centerbody of the injection duct immediately after the duct inlet due to the compressor outlet profiles of the originally designed compressor. Prior studies have demonstrated the high efficiency operating region of the G8 compressor [15, 33, 34, 35] and therefore the profile of this compressor is adopted for the FCFJ, meaning the compressor geometry is maintained but a new compressor profile is applied. Additionally, the G8 compressor swirl profile is increased by 10° to push more flow towards the sides of the injection duct to more evenly distribute flow at the outlet [36, 37]. Although the design of the compressor itself is not being iterated in this design process, there is a clear direction in which the next iteration of the compressor design should take for use with the flapped CFJ airfoil.

Table 1: Micro-compressor specifications

Design RPM	30,000
Design mass flow rate	0.165 kg/s
Design total pressure ratio	1.04
Design efficiency	84.4%
Outer Diameter	69 mm
Length	90.7 mm

3.2 CFJ Injection and Suction Ducts

In order to integrate the micro-compressor with the CFJ airfoil, the injection and suction ducts must be designed according to the following:

1. Match the mass flow requirement for the required C_μ.
2. No flow separation inside the ducts to minimize total pressure loss and maximize flow uniformity at the injection slot.
3. Maximize slot width to minimize the number of micro-compressors to be used. However, a large ratio of slot width to compressor diameter, W/D, will also make the flow easier to separate.

The injection and suction ducts are designed based on the cruise flight condition for the flapped CFJ airfoil at a flap deflection angle of $\beta = 10°$, corresponding to an AoA of 7°, at freestream Mach number 0.25. Figure 7 shows the designed ducts with a width to diameter ratio W/D of 3.26 for both the injection and suction ducts to match the micro-compressor diameter at the inlet and outlet. The injection duct has a converging area variation while the suction duct has a diverging area variation. The injection and suction ducts have a total pressure recovery of 99.4% and 99.1% respectively, shown in Figure 8. The majority of the total pressure loss of the injection duct occurs toward the outlet. The total pressure of the suction duct decreases roughly linearly throughout the length of the duct.

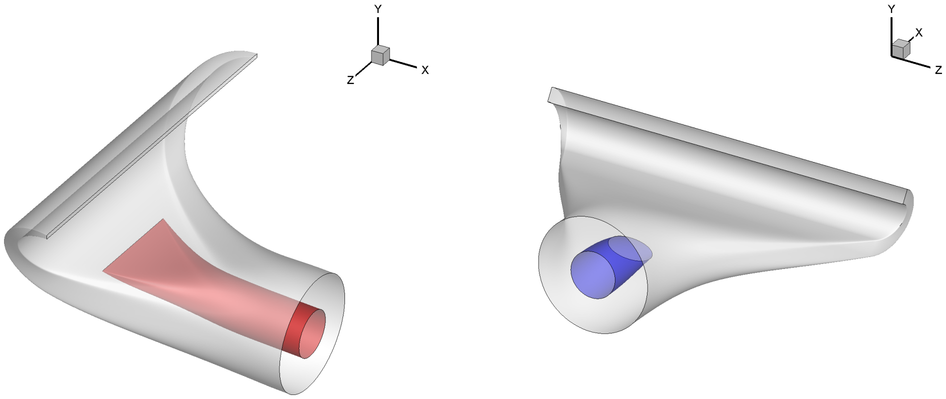

(a) (b)

Figure 7: CFJ (a)injection and (b)suction duct designed for the FCFJ airfoil

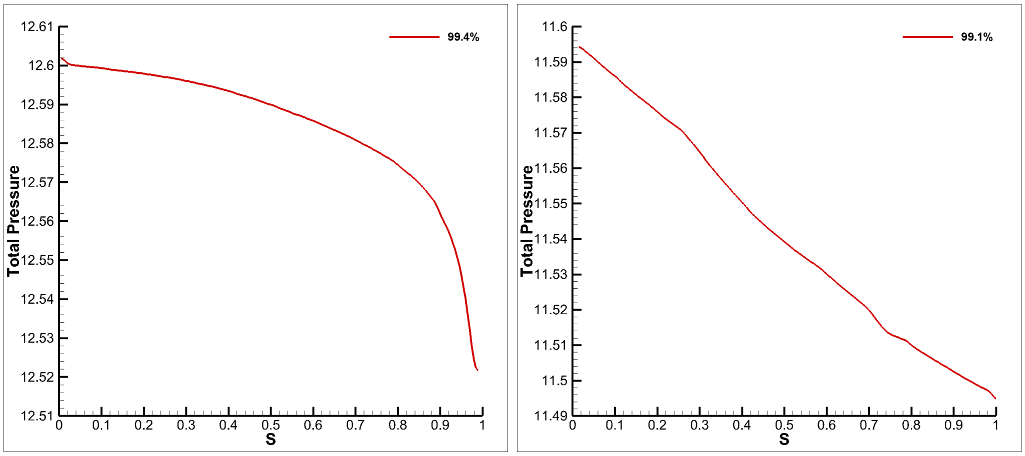

(a) (b)

Figure 8: Total pressure distribution for (a)injection and (b)suction duct designed for the FCFJ airfoil

Mach contours and streamlines are shown in Figure 9 for the injection duct. Streamlines show attached flow albeit with some weak flow near the duct and centerbody walls. The streamlines also clearly display the compressor swirl effect. Mach contours show how the flow starts at about Mach 0.1 at the inlet, staying at a range of about Mach 0.2 for the majority of the duct, and only really gains significant momentum toward the outlet where the Mach number quickly goes from about 0.3 to 0.66. This is due to the small injection slot size of 0.4%C and the small area at the slot, causing the flow to speed up substantially toward the outlet. A high speed jet will create more total pressure loss as seen in Figure 8(a) but the total pressure recovery is still significantly high.

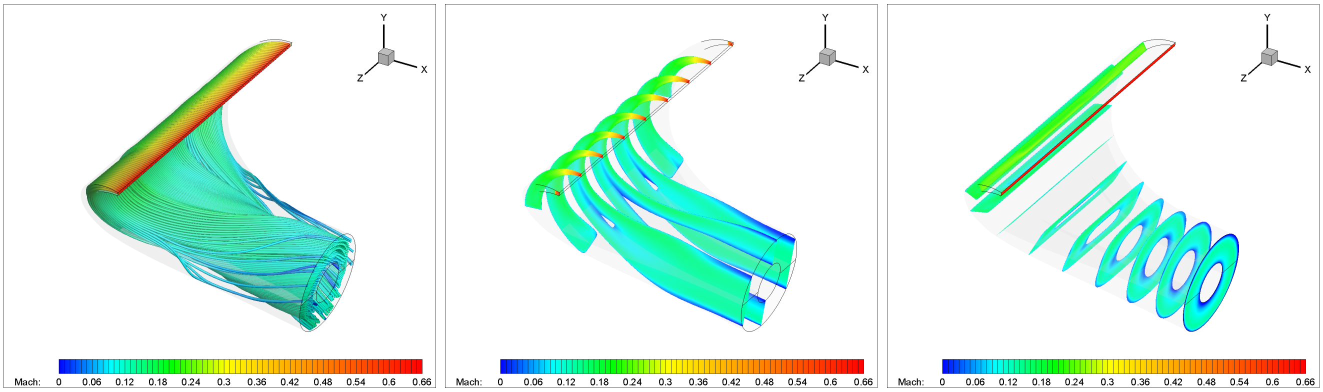

Figure 9: Mach contours and streamlines at injection duct for FCFJ airfoil at $\beta = 10°$ and Mach 0.25

Mach contours and streamlines for the suction duct are shown in Figure 10. Streamlines show separated flow at opposite ends of the suction slot at the inlet. Centrally at the inlet, the incoming streamlines are aligned with the streamwise direction, however the streamlines along the sides of the duct turn inwards to the middle after coming in contact with the duct walls, creating a swirling flow along the sides of the duct. This is the reason why the total pressure distribution of the flow decreases steadily throughout the length of the duct. The Mach contours show weak flow at the top of the duct after the turn and three regions of weak flow around the centerbody at the outlet. Streamlines under the centerbody at the outlet emanate from the sides of the suction inlet where the incoming streamwise flow collides with the duct walls and deflects to the center with spanwise velocity. The weak flow to the sides of the centerbody is caused by the swirling flow along the side walls. Improvements to the suction duct require guiding the flow toward the center to avoid the flow swirling from interactions with the duct walls. Although the total pressure recovery is high, the flow field shows multiple regions of weak flow that will affect the performance of the FCFJ airfoil and the performance of a future embedded micro-compressor. However, at this point the design process will move forward to analyze how the FCFJ airfoil performs from low speed takeoff/landing to cruise as the flap is rotated.

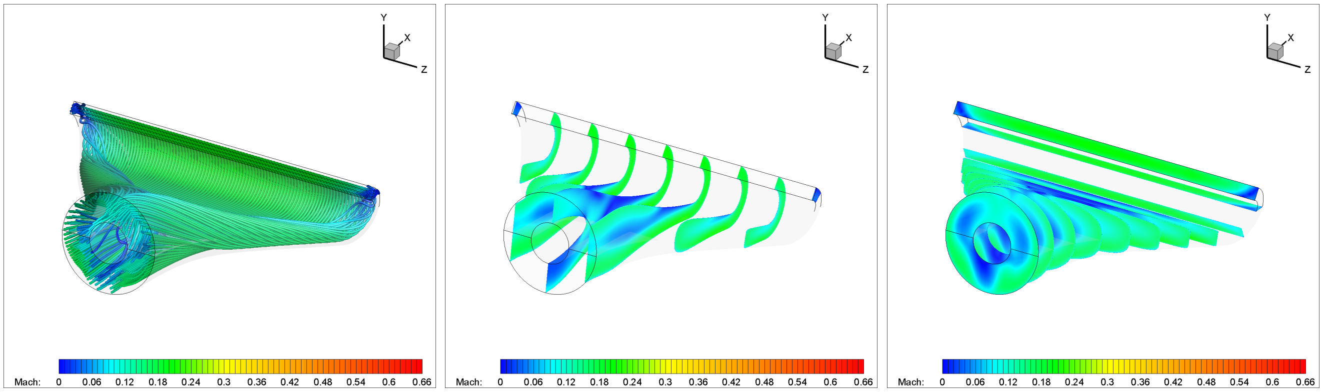

Figure 10: Mach contours and streamlines at suction duct for FCFJ airfoil at $\beta = 10°$ and Mach 0.25

3.3 Integration with FCFJ Airfoil

Once the duct design is completed, they are incorporated into the 3D FCFJ airfoil and the flow field is simulated with the external flow and the internal duct flow from low speed takeoff/landing to cruise by rotating the flap. The results of the numerical simulation analysis are shown below. Flap deflection angles $\beta = 70°$ and $60°$ are simulated at $M = 0.07$, $\beta = 50°$, $40°$, and $30°$ are simulated at $M = 0.17$, and $\beta = 20°$, $15°$, $10°$, $5°$, and $0°$ are simulated at $M = 0.25$. A minimum jet momentum coefficient C_μ is given for each β to attach the flow.

Table 2 lists the performance of the different flap angles studied, along with their equivalent AoA demonstrated by Figure 3, for each Mach number. Both the lift coefficient C_L and the drag coefficient C_D decrease as the flap angle is decreased from takeoff/landing to cruise conditions. At the Mach 0.07 takeoff/landing condition of $\beta = 70°$, the C_μ required is 0.81 in order to remove flow separation, resulting in a high power coefficient P_c of 3.557. However, it also results in a high C_L of 6.90. The highest corrected aerodynamic efficiency $(C_L/C_D)_c$ is 45.5 at $\beta = 15°$ at Mach 0.25. The selected cruise condition is $\beta = 10°$ with a corresponding AoA of 7° and a low P_c of 0.018 and a high $(C_L/C_D)_c$ of 44.6.

Table 2: Performance of the FCFJ from low speed takeoff/landing to cruise

Mach	β	$\sim AoA$	C_μ	C_L	C_D	C_M	P_c	C_L/C_D	C_L/C_{Dc}	C_L^2/C_{Dc}	P_{tr}	$\dot{m}$ (kg/s)
0.07	70°	50°	0.81	6.90	0.310	-0.306	3.557	22.3	1.8	12.4	1.33	0.174
	60°	42°	0.35	5.96	0.196	-0.255	0.896	30.4	5.5	32.5	1.12	0.110
0.17	50°	35°	0.16	4.96	0.103	-0.210	0.250	48.2	14.0	69.6	1.33	0.174
	40°	28°	0.12	4.33	0.075	-0.230	0.127	57.9	21.4	92.8	1.19	0.148
	30°	21°	0.09	3.63	0.045	-0.244	0.073	80.8	30.8	112.1	1.12	0.130
0.25	20°	14°	0.06	2.84	0.031	-0.240	0.035	90.6	42.7	121.3	1.16	0.123
	15°	10°	0.05	2.32	0.026	-0.225	0.025	89.8	45.5	105.6	1.12	0.114
	10°	7°	0.04	1.77	0.022	-0.202	0.018	82.4	44.6	79.2	1.10	0.103
	5°	4°	0.04	1.28	0.013	-0.182	0.022	95.6	36.6	46.9	1.11	0.105
	0°	0°	0.04	0.76	0.009	-0.157	0.029	84.1	20.1	15.2	1.15	0.109

The following figure describes the performance of the quasi-compressor. Figure 11(a) shows that the mass flow rate of the quasi-compressor tends to increase as β increases. At cruise Mach 0.25, for a constant C_μ, the mass flow rate decreases as the β increases because the jet velocity is increased due to greater leading edge suction peak effect. Then as the C_μ is increased, the $\dot{m}$ also increases. At Mach 0.17, the $\dot{m}$ increases with β. At low speed takeoff/landing with Mach 0.07, for $\beta = 60^\circ$ the mass flow rate is lower than at Mach 0.17 and 50° due to the freestream conditions and lower jet speed. At takeoff the mass flow rate increases with increasing β as a larger $C\mu$ is needed to remove flow separation. Figure 11(b) shows the total pressure ratio. P_{tr} increases with increasing β at each Mach number because more power is needed to overcome the adverse pressure gradients. However, at Mach 0.25, the total pressure ratio decreases from β 0° to 10° due to the decreased suction peak pressure. Figures 11(c) and (d) show the jet momentum coefficient (C_μ) and the power coefficient (P_c), respectively. Both parameters increase as the β increases and adverse pressure gradients increase. At β 70° a large C_μ is necessary to remove flow separation and hence the P_c is substantially higher than at the other conditions. At Mach 0.25, the P_c decreases slightly from β 0° to 10° due to the decrease in total pressure ratio, requiring less compressor power. Hence why $\beta = 10^\circ$ is chosen as the cruise condition, having the lowest P_c and P_{tr}.

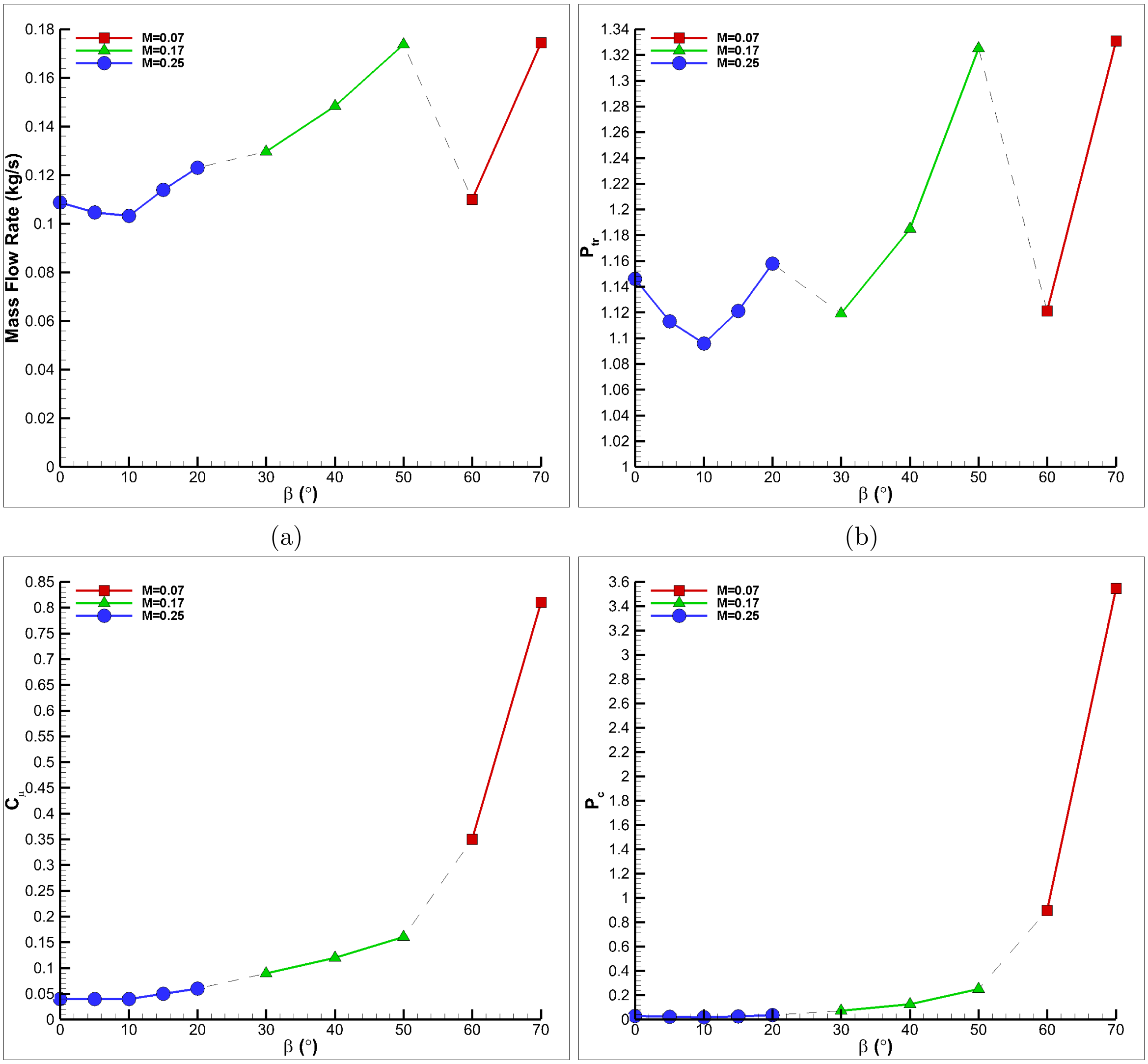

(a) (b)

(c) (d)

Figure 11: Quasi-compressor performance of (a)$\dot{m}$, (b)P_{tr}, (c)C_μ, and (d)P_c

Figure 12 shows the FCFJ airfoil aerodynamic performance. In Figure 12(a), the lift coefficient (C_L) increases roughly linearly. Highest C_L is 6.9 at the low speed takeoff/landing condition $\beta = 70°$ at Mach 0.07. The airfoil is not stalled due to the effectiveness of the co-flow jet in overcoming the extreme adverse pressure gradients. Figure 12(b) shows the drag coefficient (C_D) increasing. At cruise the drag is low. Figures 12(c) and (d) show lift to drag ratio (C_L/C_D) and corrected aerodynamic efficiency $(C_L/C_D)_c$, respectively. A high C_L/C_D of 95.6 occurs at $\beta = 5°$ and Mach 0.25, with values decreasing as the drag increases. At the highest $(C_L/C_D)_c$ of 45.5 occurs at $\beta = 15°$ and Mach 0.25, with values decreasing as β increases due to the high values of P_c.

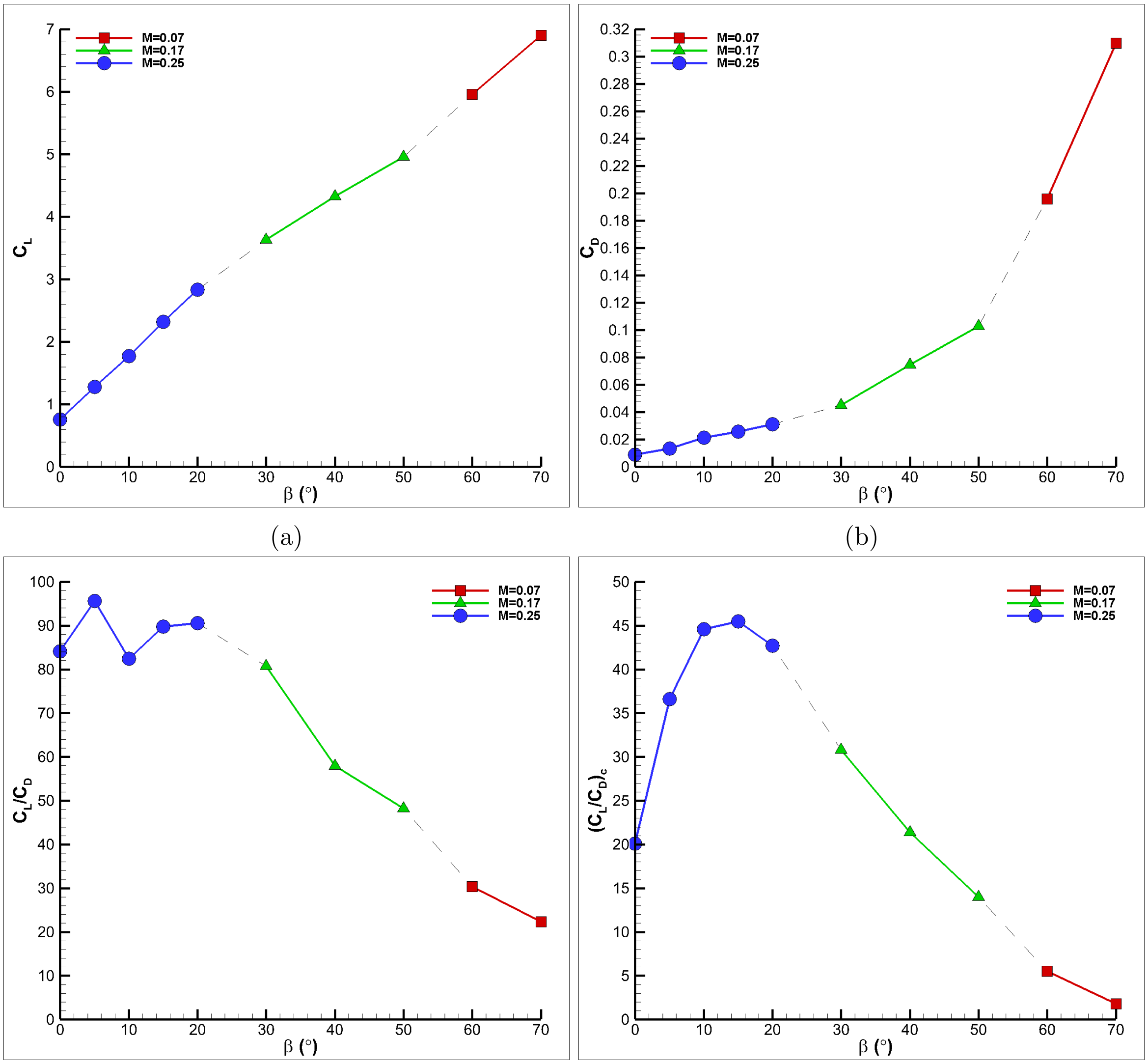

(a) (b)

(c) (d)

Figure 12: Aerodynamic performance of (a)C_L, (b)C_D, (c)C_L/C_D, and (d)C_L/C_{D_c}

The following figures show flow fields for different flap deflection angles studied. Figure 13 shows $\beta = 70°$ ($AoA = 50°$) at Mach 0.07 and $C_\mu = 0.81$ at the takeoff/landing condition. At this C_μ, streamlines show the flow is well attached overcoming adverse pressure gradients. The stagnation point is located near the trailing edge of the airfoil. At the flap location on the airfoil pressure surface, there is a vortex seen in the midspan flow field. Figure 14 shows $\beta = 60°$ ($AoA = 42°$) at Mach 0.07 and $C_\mu = 0.35$. Streamlines show flow attachment with the stagnation point shifting away from the trailing edge. Both figures show flow from the injection duct sides mixing with the main flow rather than entering the suction duct. The suction duct displays weak flow at the top of the duct toward the suction centerbody.

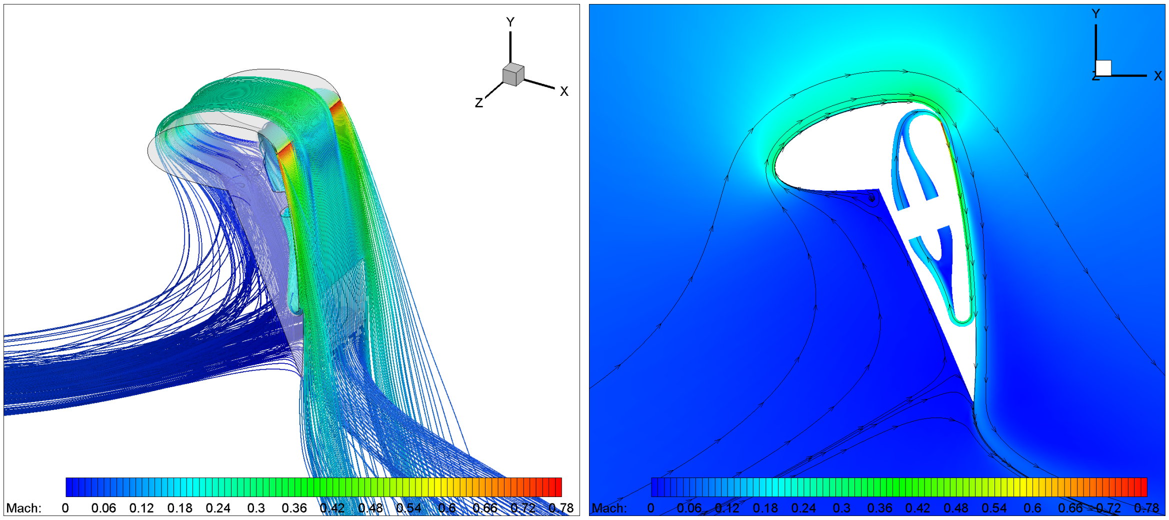

(a) (b)

Figure 13: (a)Streamlines of 3D FCFJ airfoil and (b)Mach contour flow field at 50% spanwise location of FCFJ airfoil for $\beta = 70°$ at $M = 0.07$

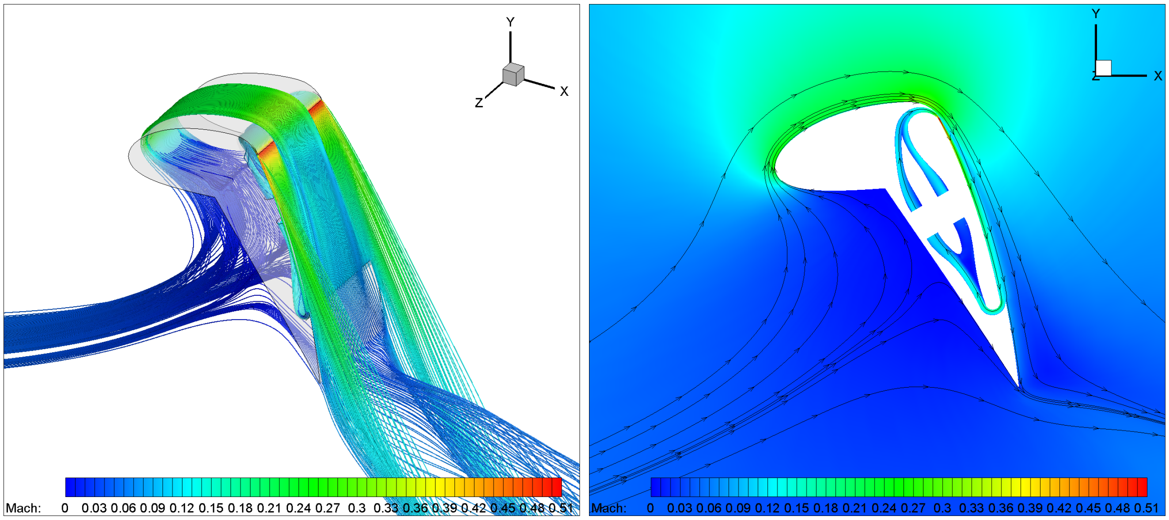

(a) (b)

Figure 14: (a)Streamlines of 3D FCFJ airfoil and (b)Mach contour flow field at 50% spanwise location of FCFJ airfoil for $\beta = 60°$ at $M = 0.07$

The Mach number is increased to $M = 0.17$. Figure 15 shows $\beta = 50°$ ($AoA = 35°$) at Mach 0.17 and $C_\mu = 0.16$. Here the injection jet is almost choked with a high Mach of 0.96 resulting in increased total pressure ratio and thus compressor power coefficient. The stagnation point is located before the flap axis of rotation near the leading edge of the airfoil. Figure 16 shows $\beta = 30°$ ($AoA = 21°$) at Mach 0.17 and $C_\mu = 0.09$. Streamlines show flow attachment except there is some flow separating at the trailing edge at either end of the airfoil segment. However, the separation is minimal and increasing the jet momentum would increase P_c and so this is deemed acceptable. The stagnation point is closer to the airfoil leading edge. The ducts in both conditions display weak flow relative to the injection jet, particularly at the top of the duct toward the suction centerbody.

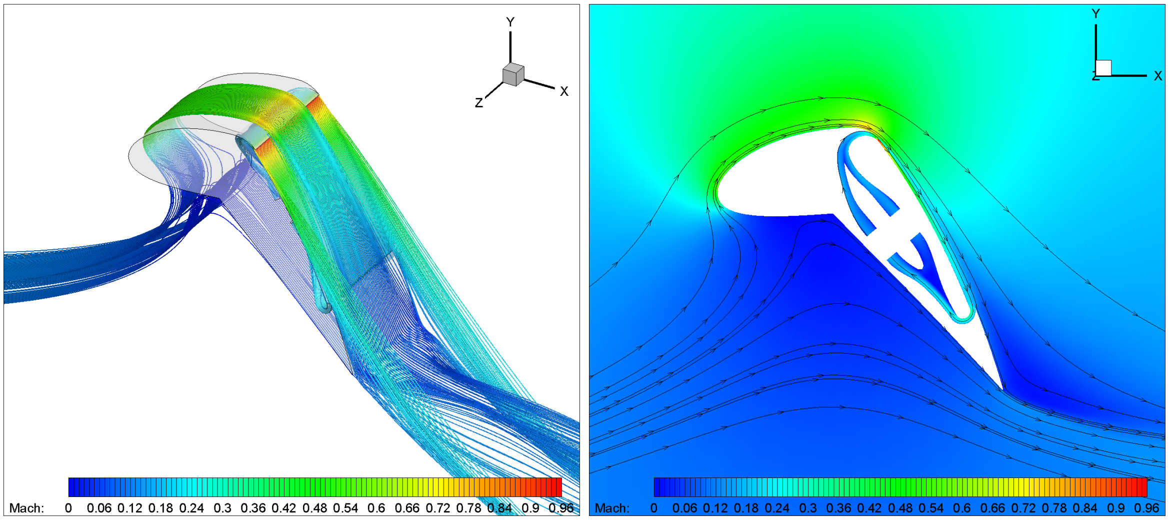

(a) (b)

Figure 15: (a)Streamlines of 3D FCFJ airfoil and (b)Mach contour flow field at 50% spanwise location of FCFJ airfoil for $\beta = 50°$ at $M = 0.17$

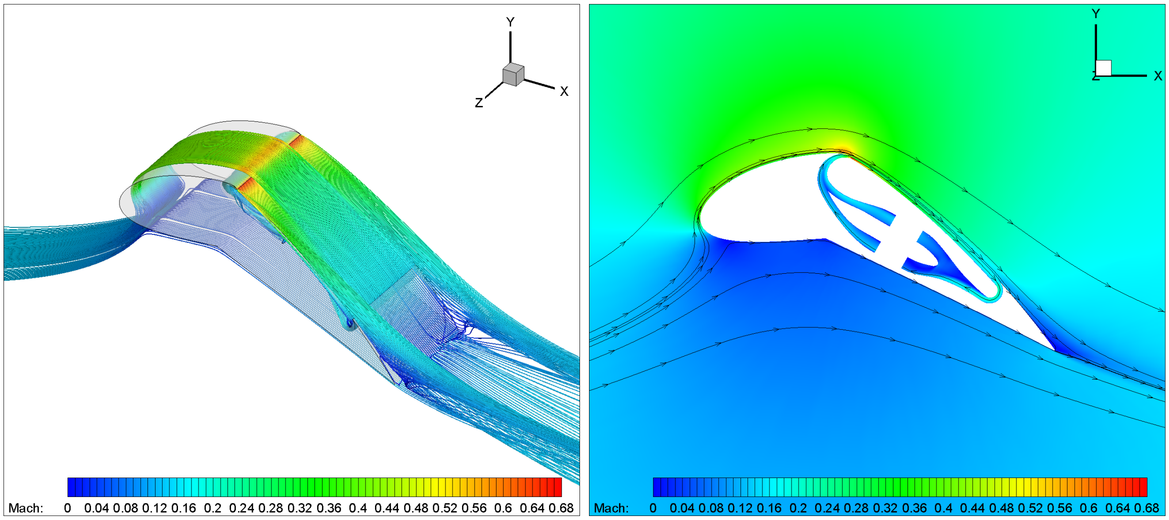

(a) (b)

Figure 16: (a)Streamlines of 3D FCFJ airfoil and (b)Mach contour flow field at 50% spanwise location of FCFJ airfoil for $\beta = 30°$ at $M = 0.17$

Figure 17 shows $\beta = 15^\circ$ ($AoA = 10^\circ$) at Mach 0.25 and $C_\mu = 0.05$ which had the best C_L/C_{D_c}. The maximum Mach number is 0.78 at the injection slot. The flow is well attached but separation occurs at the trailing edge at each side of the airfoil segment. Figure 18 shows $\beta = 10^\circ$ ($AoA = 7^\circ$) at Mach 0.25 and $C_\mu = 0.04$. This is selected as the cruise condition, with the lowest CFJ P_c achieved. The maximum Mach number is 0.66. The flow is attached but also has the separation at the sides of the trailing edge. The trailing edge side separation observed is possibly a result of the separated flow at the sides of the suction duct slot as noted in Figure 10. This weak flow seems to exit the suction slot toward the trailing edge where it then separates at the sides.

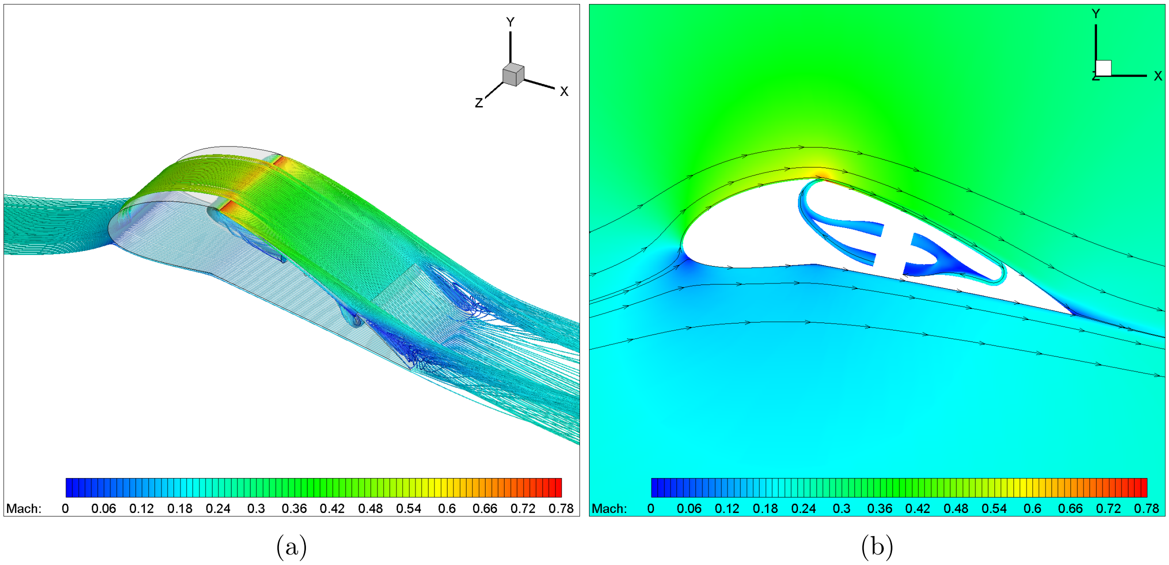

(a)

(b)

Figure 17: (a)Streamlines of 3D FCFJ airfoil and (b)Mach contour flow field at 50% spanwise location of FCFJ airfoil for $\beta = 15^\circ$ at $M = 0.25$

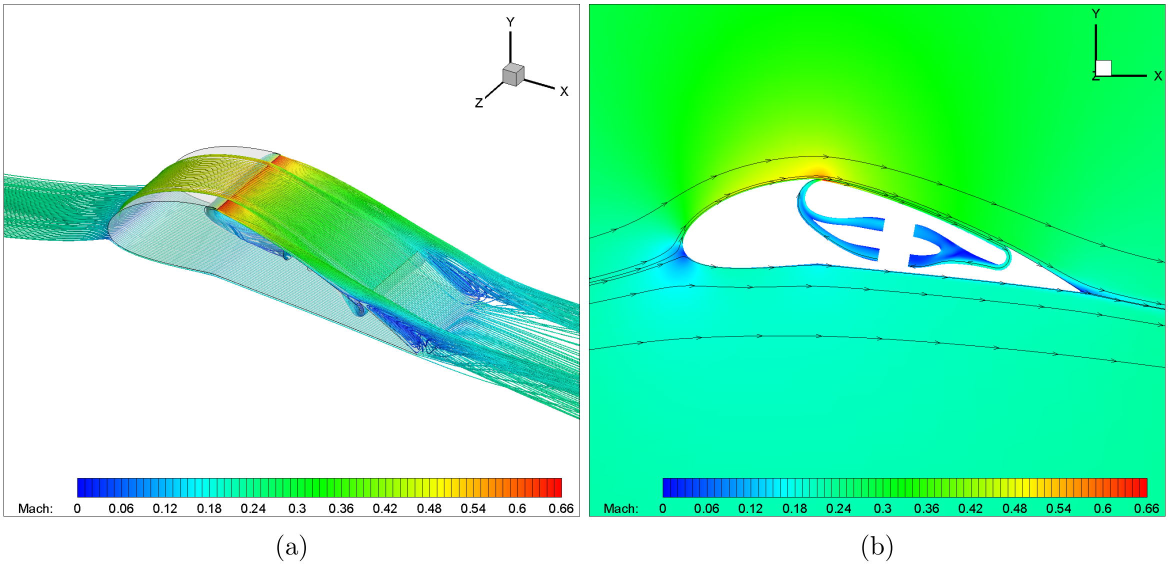

(a)

(b)

Figure 18: (a)Streamlines of 3D FCFJ airfoil and (b)Mach contour flow field at 50% spanwise location of FCFJ airfoil for $\beta = 10^\circ$ at $M = 0.25$

4 Conclusion

This paper presents a 3D flapped co-flow jet (FCFJ) airfoil with a quasi-micro-compressor to study the performance within the flight envelope from low speed takeoff/landing to cruise. The FCFJ airfoil has a flap of 60%C with CFJ on the flap as part of the airfoil. CFJ injection and suction ducts are designed for the cruise condition of Mach 0.25 with a flap deflection angle (β) of 10°, corresponding to an angle of attack (AoA) of 7°. The micro-compressor is represented by compressor boundary conditions provided by the compressor design and is therefore a quasi-micro-compressor. The purpose is to understand how the aerodynamic performance of the FCFJ varies as the airfoil flap deflection angle (β) is changed from an initial position of 70° at takeoff to 10° at cruise.

The takeoff condition is at low speed of Mach 0.07 for $\beta = 60°$ and 70°. As β is decreased from takeoff toward the cruise condition, the freestream Mach number is increased to Mach 0.17 for $\beta = 30°$, 40°, and 50°, and then to Mach 0.25 for $\beta = 0°$, 5°, 10°, 15°, and 20°. Results show a high C_L of 6.9 occurs at takeoff $\beta = 70°$ with an AoA of 50°. The lowest CFJ P_c occurs at Mach 0.25 and $\beta = 10°$, selected as the cruise condition with an AoA of 7°, with a C_L of 1.77, C_L/C_D of 89.8, $(C_L/C_D)_c$ of 44.6, and C_L^2/C_{D_c} of 79.2. The highest corrected aerodynamic efficiency (C_L/C_{D_c}) is 45.5 at cruise Mach 0.25 and $\beta = 15°$.

This study demonstrates the feasibility of using the FCFJ airfoil for the entire flight envelope with high lift coefficient for short takeoff/landing and with high aerodynamic efficiency and productivity efficiency for cruise. However, the design of the suction duct needs to be further improved by guiding the flow toward the center of the duct to avoid colliding with the duct walls and swirling inside the duct.

5 Acknowledgement

The authors would like to acknowledge the computing resources provided by the Center of Computational Sciences (CCS) at the University of Miami. The teaching assistantship support from the University of Miami is also acknowledged.

Disclosure: The University of Miami and Dr. Gecheng Zha may receive royalties for future commercialization of the intellectual property used in this study. The University of Miami is also equity owner in CoFlow Jet, LLC, licensee of the intellectual property used in this study.

References

[1] G. Zha, and C.D. Paxton, “A Novel Flow Control Method for Airfoil Performance Enhancement Using Co-Flow Jet,” *Applications of Circulation Control Technologies, AIAA Book Series, Progress in Aeronautics and Astronautics*, vol. Vol. 214, Chapter 10, pp. 293–314, 2006.

[2] G. Zha, W. Gao, and C.D. Paxton, “Jet Effects on Co-Flow Jet Airfoil Performance,” *AIAA Journal*, vol. 45, pp. 1222–1231, 2007.

[3] G.-C. Zha, C. Paxton, A. Conley, A. Wells, and B. Carroll, “Effect of Injection Slot Size on High Performance Co-Flow Jet Airfoil,” *AIAA Journal of Aircraft*, vol. 43, pp. 987–995, 2006.

[4] G.-C. Zha, B. Carroll, C. Paxton, A. Conley, and A. Wells, “High Performance Airfoil with Co-Flow Jet Flow Control,” *AIAA Journal*, vol. 45, pp. 2087–2090, 2007.

[5] Wang, B.-Y. and Haddoukessouni, B. and Levy, J. and Zha, G.-C., “Numerical Investigations of Injection Slot Size Effect on the Performance of Co-Flow Jet Airfoil,” *Journal of Aircraft*, vol. Vol. 45, No. 6,, pp. pp.2084–2091, 2008.

[6] B. P. E. Dano, D. Kirk, and G.-C. Zha, “Experimental Investigation of Jet Mixing Mechanism of Co- Flow Jet Airfoil.” AIAA-2010-4421, 5th AIAA Flow Control Conference, Chicago, IL, 28 Jun - 1 Jul 2010.

[7] B. P. E. Dano, G.-C. Zha, and M. Castillo, “Experimental Study of Co-Flow Jet Airfoil Performance Enhancement Using Micro Discreet Jets.” AIAA Paper 2011-0941, 49th AIAA Aerospace Sciences Meeting, Orlando, FL, 4-7 January 2011.

[8] A. Lefebvre, B. Dano, W. Bartow, M. Fronzo, and G. Zha, “Performance and energy expenditure of coflow jet airfoil with variation of mach number,” *Journal of Aircraft*, vol. 53, no. 6, pp. 1757–1767, 2016.

[9] A. Lefebvre and G. Zha, “Numerical simulation of pitching airfoil performance enhancement using co-flow jet flow control,” *AIAA 31st Applied Aerodynamics Conference*, vol. 2517, 2013.

[10] A. Lefebvre and G. Zha, “Co-flow jet airfoil trade study part i : Energy consumption and aerodynamic performance,” *AIAA 32nd Applied Aerodynamics Conference*, vol. 2682, 2014.

[11] A. Lefebvre and G. Zha, “Co-flow jet airfoil trade study part ii : Moment and drag,” *AIAA 32nd Applied Aerodynamics Conference*, vol. 2683, 2014.

[12] Yang, Yunchao and Zha, Gecheng, “Super-Lift Coefficient of Active Flow Control Airfoil: What is the Limit?,” *AIAA Paper 2017-1693, AIAA SCITECH2017, 55th AIAA Aerospace Science Meeting, Grapevine, Texas*, p. 1693, 9-13 January 2017.

[13] G.-C. Zha, Y.-C. Yang, Y. Ren, and B. McBreen, “Super-lift and thrusting airfoil of coflow jet-actuated by micro-compressors.” AIAA Paper 2017-3061, AIAA AVIATION 2018, Atlanta, GA, Submitted for publication in AIAA Journal , 25 - 29 June 2018.

[14] Y. Wang and G.-C. Zha, “Study of Mach Number Effect for 3D Co-Flow Jet Wings at Cruise Conditions.” AIAA Paper 2020-0045, AIAA SciTech 2020, AIAA SciTech 2020 Forum, Orlando, Florida, 6-10 January 2020.

[15] *Simulation of 3D Co-Flow Jet Airfoil Control with Micro-Compressor Actuator at High Angles of Attack*, 12-16 June 2023.

[16] Y. Wang, Y.-C. Yang, and G.-C. Zha, “Study of Super-Lift Coefficient of Co-Flow Jet Airfoil and Its Power Consumption.” AIAA Paper 2019-3652, AIAA Aviation 2019, AIAA Applied Aerodynamics Conference, Dallas, Texas, 17-21 June 2019.

[17] J. Jeon, Y. Ren, and G.-C. Zha, “Toward Ultra-High Cruise Lift Coefficient Using Flapped CoFlow Jet Airfoil.” AIAA SciTech 2023, AIAA SciTech Forum 2023, National Harbor, Maryland, 23-27 Jan 2023.

[18] *Feasibility Study of Deflected Slipstream Airfoil for VTOL Hover Enabled by CoFlow Jet*, 12-16 June 2023.

[19] K. Xu, Y. Ren, and G.-C. Zha, “Separation Control by Co-Flow Wall Jet.” AIAA Paper 2021-2946, AIAA Aviation 2021, AIAA Aviation Forum 2021, 2-6 Aug 2021.

[20] Y. Ren and G.-C. Zha, “Design of Injection and Suction Ducts for Co-Flow Jet Airfoils with Embedded Micro-Compressors Actuator.” AIAA Aviation Forum, 2018 Flow Control Conference, Atlanta, Georgia, 25-29 June 2018.

[21] Y. Wang and G.-C. Zha, “Study of 3D Co-flow Jet Wing Induced Drag and Power Consumption at Cruise Conditions.” AIAA Paper 2019-0034, AIAA SciTech 2019, San Diego, CA, January 7-11, 2019.

[22] Y. Wang and G.-C. Zha, “Study of Mach Number Effect for 2D Co-Flow Jet Airfoil at Cruise Conditions.” AIAA Paper 2019-3169, AIAA Aviation 2019, AIAA Applied Aerodynamics Conference, Dallas, Texas, 17-21 June 2019.

[23] P. R. Spalart and S. R. Allmaras, “A one-equation turbulence model for aerodynamic flows,” in *30th Aerospace Sciences Meeting and Exhibit, Aerospace Sciences Meetings, Reno, NV, USA, AIAA Paper 92-0439*, 1992.

[24] Shen, Y.Q., and Zha, G.C., “Large Eddy Simulation Using a New Set of Sixth Order Schemes for Compressible Viscous Terms,” *Journal of Computational Physics*, vol. 229, pp. 8296–8312, doi:10.1016/j.jcp.2010.07.017, 2010.

[25] Zha, G.C., Shen, Y.Q. and Wang, B.Y., “An improved low diffusion E-CUSP upwind scheme ,” *Journal of Computer and Fluids*, vol. 48, pp. 214–220, Sep. 2011.

[26] Y.-Q. Shen and G.-Z. Zha , “Generalized finite compact difference scheme for shock/complex flowfield interaction,” *Journal of Computational Physics*, vol. doi:10.1016/j.jcp.2011.01.039, 2011.

[27] Shen, Y.Q., Zha, G.C., and Wang, B.Y., “Improvement of Stability and Accuracy of Implicit WENO Scheme,” *AIAA Journal*, vol. 47, pp. 331–334, DOI:10.2514/1.37697, 2009.

[28] Shen, Y.Q., Zha, G.C., and Chen, X., “High Order Conservative Differencing for Viscous Terms and the Application to Vortex-Induced Vibration Flows,” *Journal of Computational Physics*, vol. 228(2), pp. 8283–8300, doi:10.1016/j.jcp.2009.08.004, 2009.

[29] Shen, Y.Q., and Zha, G.C., “Improvement of the WENO Scheme Smoothness Estimator,” *International Journal for Numerical Methods in Fluids*, vol. 64,, pp. 653–675, DOI:10.1002/fld.2186, 2009.

[30] Zha, G.C., and Bilgen, E., “Numerical Study of Three-Dimensional Transonic Flows Using Unfactored Upwind Relaxation Sweeping Algorithm,” *Journal of Computational Physics*, vol. 125, pp. 425–433,, 1996.

[31] Wang, B.Y., Hu, Z. and Zha, G.C., “A General Sub-Domain Boundary Mapping Procedure For Structured Grid CFD Parallel Computation,” *AIAA Journal of Aerospace Computing, Information, and Communication*, vol. 5, pp. 425–447, 2008.

[32] Y.-Q. Shen, G.-C. Zha, and B.-Y. Wang, “Improvement of Stability and Accuracy of Implicit WENO Scheme,” *AIAA Journal*, vol. 47, pp. 331–344, 2009.

[33] Y. Ren, P. Barrios, and G.-C. Zha, “Simulation of 3D Co-Flow Jet Airfoil with Integrated Micro-Compressor Actuator.” AIAA Paper 2022-3553, AIAA Aviation 2022, AIAA Aviation 2022 Forum, Chicago, Illinois, 27-1 July 2022.

[34] P. Barrios, Y. Ren, and G.-C. Zha, “Simulation of 3D Co-Flow Jet Airfoil with Integrated Micro-Compressor Actuator at Different Cruise Flight Conditions.” AIAA SciTech 2023, AIAA SciTech 2023 Forum, National Harbor, Maryland, 23-27 Jan 2023.

[35] Y. Ren, K. Xu, and G.-C. Zha, “Design of G8 Micro-Compressor for CoFlow Jet Airfoil.” Internal Report No.1, Dept. of Mechanical and Aerospace Engineering, University of Miami, May 2020.

[36] Y. Ren and G.-C. Zha, “Simulation of 3D Co-Flow Jet Airfoil with Embedded Micro-Compressor Actuator.” AIAA Paper 2018-0330, 2018 AIAA Aerospace Sciences Meeting, AIAA SciTech Forum, Kissimmee, Florida, 8-12 January 2018.

[37] P. Barrios, Y. Ren, and G.-C. Zha, “Design of High Width-Diameter Ratio Injection and Suction Ducts for Co-Flow Jet Airfoil.” AIAA Paper 2022-3772, AIAA Aviation 2022, AIAA Aviation 2022 Forum, Chicago, IL, 27 June - 1 July 2022.